Systematic Methodology for the Global Stability Analysis of Nonlinear Circuits

Silvia Hernández, *Student Member, IEEE*, Almudena Suárez, *Fellow, IEEE*

***Abstract*—A new methodology for the detection of Hopf, flip and turning-point bifurcations in nonlinear circuits analyzed with harmonic balance is presented. It enables a systematic determination of bifurcation loci in terms of relevant parameters, such as input power, input frequency and bias voltages, for instance. It does not rely on the use of continuation techniques and is able to globally provide the entire loci, often containing multi-valued sections and/or disconnected curves, in a single simulation. The calculation of Hopf and flip bifurcations is based on the extraction of a small-signal admittance/impedance function from harmonic balance and the calculation of its zeroes through a geometrical procedure. The method is ideally suited for the investigation of the global stability properties of power amplifiers and other nonlinear circuits. The turning-point locus, associated with either jump phenomena or synchronization, is obtained taking into account the annihilation/generation of steady-state solutions that is inherent to this type of bifurcation. A technique is also presented for the exhaustive calculation of oscillation modes in multi-device oscillators and oscillators loaded with multi-resonance networks. The new methodologies are illustrated through their application to a power amplifier and a multi-mode oscillator.**

***Index Terms*—Stability, bifurcation, oscillation, harmonic balance**

I. Introduction

INSTABILITIES are a major concern in power amplifiers and other active circuits [1]-[5], which often exhibit undesired behavior, such as frequency divisions by two, oscillations at incommensurable frequencies or hysteresis [6]-[9]. These phenomena arise through different types of bifurcations [6]-[10], or qualitative changes in the solution stability or the number of steady-state solutions when a parameter is varied continuously [11]-[15]. There are three main methodologies for the prediction of the stability properties at the simulation stage: the Nyquist analysis, applied to the system characteristic determinant [6]-[7], [10], the Nyquist analysis, applied to the normalized determinant function [3], [16]-[17], and pole-zero identification [1]-[2], [18]-[19], applied to a closed-loop transfer function, associated with the circuit linearization about the particular steady-state solution. Only the last two methods are compatible with the use of commercial harmonic balance (HB). On the other hand, the unstable-behavior regions [4]-[5], [7], [20]-[24] in terms of relevant parameters, such as the input power, input frequency or bias voltages, can be efficiently determined through bifurcation detection. In comparison with the stability analysis, one advantage of the bifurcation analysis is that the critical poles are purely imaginary or zero at the bifurcation points, so their detection relies on standard simulation methods based on real frequencies.

When using commercial software, the bifurcation analysis can be carried out with auxiliary generators (AGs) operating under certain conditions [4]-[5], [8]-[9], which depend on the kind of bifurcation to be detected. The Hopf and flip bifurcations [20], respectively associated with the onset of incommensurable oscillations and frequency divisions by two, are calculated taking into account that ordinary oscillations are generated/extinguished with amplitude tending to zero [21]. They are detected by introducing a small-signal AG into the circuit, operating at the oscillation frequency, and solving for the parameter values at the limit oscillation condition [20], given by the zero value of the ratio between the current and voltage of the small-signal AG.

The detection of turning points bifurcations, associated with either jump phenomena or synchronization [5], [21], is more demanding. The circuit operates in nonlinear regime with respect to the AG, and the turning-point condition is given by the singularity of the Jacobian matrix of the AG admittance function [21]. In commercial HB, the derivatives in this matrix are obtained applying finite differences to the AG at each iteration of the optimization procedure [5]. This should provide the parameter values for both a zero value of the AG current-to-voltage ratio and a zero value of the determinant of the Jacobian matrix [5], which is numerically involved.

When using commercial software, the bifurcation loci in terms of two significant parameters, η_1 and η_2 is obtained through optimization plus parameter switching. One of the parameters (η_1) is swept, solving the particular bifurcation condition through optimization, in terms of the AG variable(s) and the parameter η_2, at each sweep step [20], [25]. There can be two different problems associated with this procedure. One is the usual existence of infinite-slope points versus η_1, which would demand a manual parameter switching by the user to η_2 or the AG frequency or phase, depending on the type of bifurcation. Another problem is the possible existence of

This work was supported by the Spanish Ministry of Economy and Competitiveness and the European Regional Development Fund (ERDF/FEDER) under the research project TEC2017-88242-C3-1-R.

The authors are with Dpto. Ingeniería de Comunicaciones, Universidad de Cantabria., Av. Los Castros 39005, Santander, Spain (e-mail: silvia.hernandez@unican.es; almudena.suarez@unican.es).

disconnected locus curves, which cannot be predicted through continuation techniques (even in in-house software).

In this work a new method for bifurcation analysis is proposed, which, unlike previous ones, is systematic. It efficiently provides multiple locus sections, and even disconnected locus curves, with no need for continuation procedures, such as parameter switching. The new method is based on the introduction of a small-signal AG in the HB software. However, this AG is not used to impose a bifurcation condition, solved through optimization, as done in previous works [20], [25], but to extract a small-signal admittance or impedance function. This function is analyzed through contour plots in a dedicated in-house software. This way all the bifurcation points existing for a given value of η_1, in terms of the other parameter η_2 (and the AG frequency or phase), are obtained simultaneously, regardless of the distance between these points, in terms of the analysis variables. The procedure is extended to obtain autonomous and subharmonic solution curves versus a parameter η. The turning-point bifurcations are calculated taking into account that these points are characterized by the annihilation/generation of two steady-state solutions in a solution curve [6], [22].

The new methodology will enable an exhaustive search of free-running oscillations in symmetric multi-device topologies [26]-[29] and circuits loaded with multi-resonance networks, such as reconfigurable oscillators or crystal oscillators [29]. These circuits often exhibit multiple oscillation modes, which are difficult to detect and control, due to their inherent autonomy and the bifurcation phenomena involved in their generation. In previous works [27]-[28], each mode is analyzed in HB individually. Here, the new geometrical method will enable a systematic solution search in given intervals of oscillation amplitude and frequency. Due to their ease of application, we believe that the new methodologies can be very helpful for nonlinear-circuit designers.

The paper is organized as follows. Section II presents the bifurcation detection from dc regime. Section III describes the calculation of multivalued solution curves. Section IV presents the procedures to obtain the flip, Hopf and turning-point bifurcation loci.

II. BIFURCATION LOCI FROM DC REGIME

Due to the usual decoupling of dc signals in microwave circuits, the most common type of bifurcation from dc regime is the primary Hopf bifurcation [6]-[9]. At this bifurcation, and when varying continuously a circuit parameter η, a pair of complex-conjugate poles $\sigma \pm j\omega$ crosses the imaginary axis, which gives rise to the onset or extinction of a free-running oscillation.

A. Analysis method

The exhaustive detection of primary Hopf bifurcations is carried out through a methodology in two stages. The first stage is the extraction of a small-signal admittance or impedance function (Y_s or Z_s) from the microwave-circuit simulation software. This function must be evaluated versus the two analysis parameters, η_1 and η_2, and the possible oscillation frequency, ω. The second stage is the simultaneous calculation of the zeroes of this function through a geometrical procedure [30] that does not rely on continuation.

Without loss of generality, the case of an admittance function Y_s will be considered. To obtain Y_s, a small-signal current source I_s will be connected in parallel at a sensitive circuit node, such as a device terminal. The source I_s operates at the unknown oscillation frequency ω. The function Y_s is calculated as the ratio $Y_s = I_s/V_s$, where V_s is the node voltage at ω.

To obtain the primary-Hopf locus versus the two parameters η_1 and η_2, a nested sweep is carried out in η_1, η_2 and ω, evaluating the admittance Y_s at each step. The ω sweep will go from near zero to the transistor maximum operating frequency. Thus, for each η_1, one will have the two-entry function $Y_s^{\eta_1}(\omega_p, \eta_{2,n})$, where the superscript indicates the particular η_1 value and the subscripts are counters of the double sweep, such that p (going from 1 to P) indicates the point of the ω sweep and n (going from 1 to N) indicates the point of the inner η_2 sweep. The exported admittance function is split into real and imaginary parts and the data are structured in two matrices:

$$Y_{s,r}^{\eta_1}\left(\omega_p, \eta_{2,n}\right),\ \ Y_{s,i}^{\eta_1}\left(\omega_p, \eta_{2,n}\right) \qquad p = 1...P,\ n = 1...N \tag{1}$$

where the additional subscripts r and i indicate real and imaginary parts. Then, the discrete functions in (1) are interpolated. Linear interpolation is preferred to avoid any possible generation of artificial resonances in the frequency intervals with a significant variation of Y_s. The interpolation leads to the new functions, $Y_{s,r}^{\eta_1}(\omega, \eta_2)$, $Y_{s,i}^{\eta_1}(\omega, \eta_2)$, given by:

$$Y_{s,r}^{\eta_1}(\omega,\eta_2) = \frac{\left[\omega_{p+1}-\omega \quad \omega-\omega_{p+1}\right]}{(\omega_{p+1}-\omega_p)(\eta_{2,n+1}-\eta_{2,n})} \cdot \begin{bmatrix} Y_{\eta_1}^r(\omega_p,\eta_{2,n}) & Y_{\eta_1}^r(\omega_p,\eta_{2,n+1}) \\ Y_{\eta_1}^r(\omega_{p+1},\eta_{2,n}) & Y_{\eta_1}^r(\omega_{p+1},\eta_{2,n+1}) \end{bmatrix} \begin{bmatrix} \eta_{2,n+1}-\eta_2 \\ \eta_2-\eta_{2,n} \end{bmatrix}$$

$$Y_{s,i}^{\eta_1}(\omega,\eta_2) = \frac{\left[\omega_{p+1}-\omega \quad \omega-\omega_{p+1}\right]}{(\omega_{p+1}-\omega_p)(\eta_{2,n+1}-\eta_{2,n})} \cdot \begin{bmatrix} Y_{\eta_1}^i(\omega_p,\eta_{2,n}) & Y_{\eta_1}^i(\omega_p,\eta_{2,n+1}) \\ Y_{\eta_1}^i(\omega_{p+1},\eta_{2,n}) & Y_{\eta_1}^i(\omega_{p+1},\eta_{2,n+1}) \end{bmatrix} \begin{bmatrix} \eta_{2,n+1}-\eta_2 \\ \eta_2-\eta_{2,n} \end{bmatrix} \tag{2}$$

$$\omega_p \le \omega < \omega_{p+1},\ \ \eta_{2,n} \le \eta_2 < \eta_{2,n+1}$$

At each η_1, the Hopf bifurcations will fulfill $Y_s^{\eta_1}(\omega, \eta_2) = 0$. Setting $Y_{s,r}^{\eta_1}(\omega, \eta_2) = 0$, and solving for $\eta_2(\omega)$, one obtains a contour plot in the plane (ω, η_2), denoted as $F_r(\eta_1) = \eta_{2,r}(\eta_1, \omega)$. Likewise, setting $Y_{s,i}^{\eta_1}(\omega, \eta_2) = 0$, and solving for $\eta_2(\omega)$, one obtains the contour plot $F_i(\eta_1) = \eta_{2,i}(\eta_1, \omega)$. All the Hopf-bifurcation points coexisting for η_1 are given by the intersections between these two contour plots, calculated from the equation:

$$\eta_{2,r}(\eta_1, \omega) = \eta_{2,i}(\eta_1, \omega) \tag{3}$$

Note that the above equation can have one or more solutions, i.e., there can be one or more Hopf bifurcations for each η_1. In a compact manner, the intersection points will be denoted as:

$$\left[\omega_H(\eta_1), \eta_{2,H}(\eta_1)\right] = F_r(\eta_1) \cap F_i(\eta_1) \quad (4)$$

One obtains the primary-Hopf locus by sweeping η_1 and representing the solutions of (4) in the plane (η_1, η_2) or the plane (η_1, ω). When obtaining multiple intersection points (ω, η_2) in a certain η_1 interval, the locus will be composed by several sections, as in the case of a folded locus, or by two or more disconnected curves. None of this constitutes an analysis difficulty, since the intersection (4) simultaneously provides all the locus points coexisting for η_1, regardless of the distances between these points.

B. Application to a power amplifier

The above procedure has been applied to a demonstrator power-combining amplifier, shown in Fig. 1. Note that the purpose of this prototype is not to obtain a very performant design but to exhibit a variety of instability phenomena, enabling an illustration of the capabilities of the new analysis methodologies. The demonstrator is based on the transistor ATF-34143 and is expected at 3 GHz.

The procedure in (1) to (4) has been used to detect the primary Hopf bifurcations of this amplifier. Initially, the auxiliary current source I_s, used for the extraction of the admittance function, is connected to the drain terminal of one of the two transistors. The parameters considered are the gate-bias voltage V_{GS} and the drain-bias voltage V_{DS}. Fig. 2(a) shows the family of contours $F_r(\eta_1)$, $F_i(\eta_1)$ obtained when sweeping $\eta_1 = V_{DS}$ in the interval 0 V to 4 V, with a step of 0.1 V. The parameter η_2, used in the contour calculation, is $\eta_2 = V_{GS}$. It is swept in the interval –1 V to 0 V, with a step of 0.025 V. The grey (cyan) contours correspond to $F_r(\eta_1)$ [$F_i(\eta_1)$]. Note that, for $V_{DS} = 0$, $Y_{s,r}^{\eta_1}(\omega, \eta_2) = 0$ and $Y_{s,i}^{\eta_1}(\omega, \eta_2) = 0$ are not fulfilled, thus there are not contour plots. The intersection points $[\omega_H(\eta_1), \eta_{2,H}(\eta_1)]$, marked with circles, constitute the primary-Hopf bifurcation points versus V_{GS} and V_{DS}. The intersection points in the plane (ω, η_2) provide immediate information on the oscillation frequency, which in the case of the circuit in Fig. 1 is comprised between 1.22 GHz to 1.38 GHz.

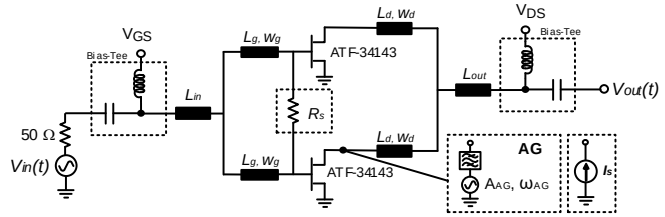

(a)

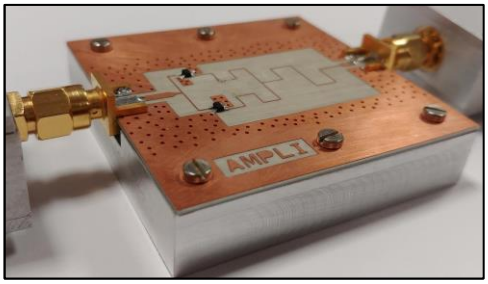

(b)

Fig. 1. Amplifier based on transistor ATF-34143, expected to operate at 3 GHz. (a) Schematic of amplifier. The lengths of the transmission lines are L_{in} = 1.15 mm, L_g = 9 mm, L_d = 26 mm, L_{out} = 40 mm. The small-signal current source I_s used for the detection of primary-Hopf bifurcations is shown in a box. The AG used for the bifurcation analysis from periodic regime and for the calculation of solution curves is shown in another box. (b) Photograph of the manufactured prototype.

Fig. 2(b) shows the primary-Hopf bifurcation locus in the plane (V_{GS}, V_{DS}), with the experimental points at the oscillation boundary superimposed. For V_{GS} below conduction ($V_{GS} < -0.81$ V), the dc solution is necessarily stable, so the unstable region should correspond to the inside of the locus, as confirmed by the measurements. When connecting the current source I_s to the gate terminal one obtains the same Hopf-locus points, superimposed in Fig. 2(b). This is because the bifurcation condition $Y_s = 0$ is fulfilled at all the circuit nodes, so there will be no dependence on the analysis node, provided that the node enables a sufficient observability.

Fig. 2(c) presents an additional validation of the locus points through pole-zero identification [1]-[2]. Two different values of V_{GS} have been considered, $V_{GS} = -0.25$ V and $V_{GS} = -0.5$ V. In the two cases, the amplifier is stable for very low V_{DS}. Increasing this voltage, a pair of complex-conjugate poles crosses from the left-hand side of the complex plane (LHS) to the right-hand side (RHS), in a direct Hopf bifurcation. For $V_{GS} = -0.5$ V, the poles cross to the RHS at $V_{DS} = 0.7$ V, which corresponds to the Hopf bifurcation H_1. For $V_{GS} = -0.25$ V, the poles cross to the RHS at $V_{DS} = 1$ V, which corresponds to the Hopf bifurcation H_2. The two bifurcations are well predicted by the Hopf locus in Fig. 2(b), as indicated with the two arrows showing the interval and sense of variation of V_{DS} in the pole-zero identification (at $V_{GS} = -0.5$ V and $V_{GS} = -0.25$ V).

One relevant advantage of the new method is that it enables a global exploration of the circuit global stability properties through a simple inspection of the contours $F_r(\eta_1)$ and $F_i(\eta_1)$. The parameter sweeps should include intervals in which the transistor is necessarily stable, for instance V_{GS} below the conduction threshold or $V_{DS} = 0$ V. Then, one can ensure that the amplifier is stable for all the possible parameter combinations if no intersection points between the two contours are obtained. Thus, the method is very powerful to assess the small-signal stability of a particular design.

To illustrate this, a stabilization resistor R_s will be connected between the transistor gates. Fig. 2(d) presents the contours $F_r(\eta_1)$, $F_i(\eta_1)$ for $R_s = 450\ \Omega$, showing very few intersection points. As the resistor value decreases, the region of these intersection points decreases too and with the standard value $R_s = 51\ \Omega$, the contours $F_r(\eta_1)$, $F_i(\eta_1)$ do not even exist. To illustrate the effect of R_s on the Hopf locus, Fig. 2(b) includes the loci obtained for $R_s = 500\ \Omega$ (purple) and $R_s = 450\ \Omega$ (green). The unstable region decreases with R_s. In the experimental characterization $R_s = 51\ \Omega$ has been chosen to ensure not only stable behavior, but also a sufficient stability margin.

The unstable spectrum obtained experimentally for $V_{GS} = -0.6$ V, $V_{DS} = 1.5$ V and $P_{in} = -30$ dBm without a stabilization resistor is shown in Fig. 3(a). The stable spectrum obtained experimentally with the stabilization resistor $R_s = 51\ \Omega$ is shown in Fig. 3(b). With this resistor, and for $V_{GS} = -0.7$ V, $P_{in} = 3.98$ dBm, the amplifier exhibits an output

power P_{out} = 10 dBm and an efficiency of 20%. The output spectrum is shown in Fig. 3(c).

Although the instability of the power amplifier could easily be suppressed with the aid of R_s, this resistor will not be used in the subsequent large-signal stability analyses of this amplifier. This is because the aim is to demonstrate the capability of the new methodologies to detect a variety of instability phenomena.

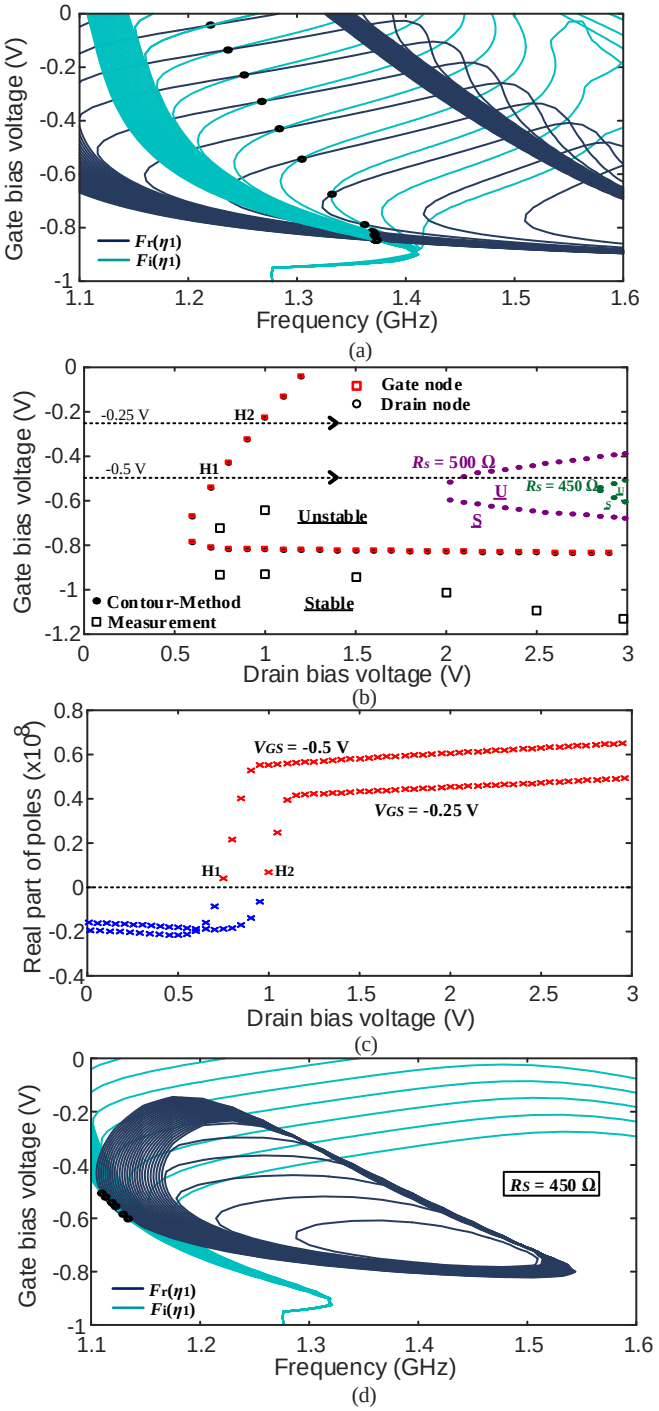

Fig. 2. Primary-Hopf bifurcation locus in the plane defined by $\eta_1 = V_{DS}$ and $\eta_2 = V_{GS}$. (a) Family of contours $F_r(\eta_1)$, $F_i(\eta_1)$ obtained when sweeping η_1, and intersection points $[\omega_H(\eta_1),\eta_{2,H}(\eta_1)]$, corresponding to the primary-Hopf bifurcations, in the plane defined by ω and $\eta_2 = V_{GS}$. (b) Bifurcation locus with experimental points at the oscillation boundary. The bifurcation loci obtained for R_s = 500 Ω and R_s = 450 Ω are also represented. (c) Validation of the locus points by means of pole-zero identification for the two V_{GS} values, indicated with arrows in (b). (d) Contour plots $F_r(\eta_1)$, $F_i(\eta_1)$ with the stabilization resistor R_s = 450 Ω, showing very few intersection points.

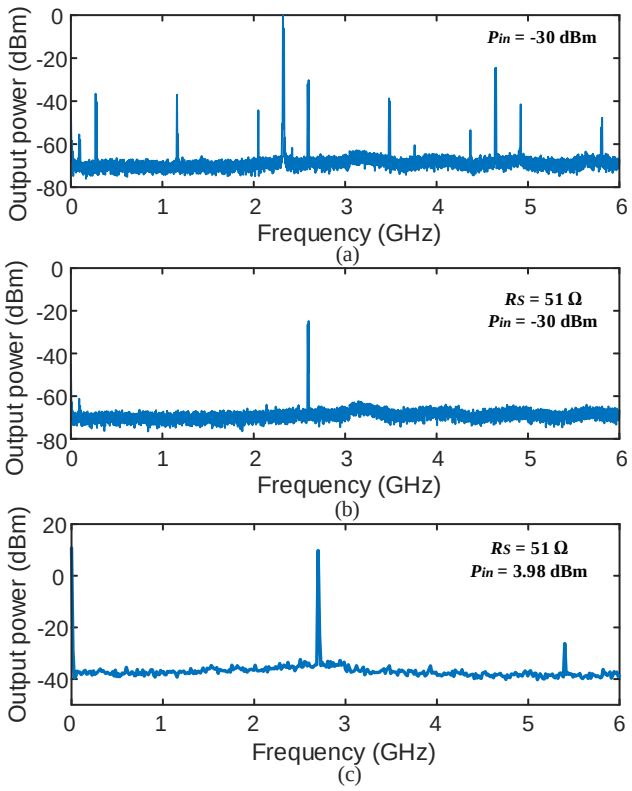

Fig. 3. Experimental measurements of the power amplifier. (a) Output spectrum at V_{GS} = –0.6 V and V_{DS} = 1.5 V, with P_{in} = –30 dBm, without a stabilization resistor (unstable). (b) With a stabilization resistor R_s = 51 Ω, connected between the gate terminals (stable). (c) Output spectrum at V_{GS} = –0.7 V, for P_{in} = 3.98 dBm.

C. Application to a multi-mode oscillator

The method will also be illustrated through its application to the ring oscillator in Fig. 4, susceptible to oscillate at different modes. It is based on the transistor ATF-34143. As will be shown, it exhibits primary Hopf bifurcations around four frequencies: 1.2 GHz, 1.6 GHz, 2.6 GHz and 4.5 GHz.

For the analysis of the primary Hopf bifurcations, a small-signal current source I_s is connected to the drain of one of the transistor devices (Fig. 4). The corresponding loci are calculated versus the gate bias voltage $\eta_2 = V_{GS}$ and the tuning voltage of the varactor diode $\eta_1 = V_D$. Fig. 5(a) presents the intersection points $[\omega_H(\eta_1),\eta_{2,H}(\eta_1)]$ obtained through a coarse frequency sweep. The diagram shows three clusters of points, around 1.5 GHz, 2.6 GHz and 4.5 GHz, corresponding to the primary Hopf bifurcations. Thus, the method is capable to predict instabilities at largely spaced frequencies. In fact, it is able to detect all the possible oscillation modes in the interval considered in the frequency sweep. Once the oscillation modes have been detected through the above coarse sweep, the bifurcation loci are calculated through a finer sweep about each detected frequency.

The resulting loci are shown in Fig. 5(b). For each oscillation mode there is a distinct locus curve, so one can immediately know the parameter values (V_D, V_{GS}) at which each mode is generated or extinguished. The oscillation frequency corresponding to each mode is indicated, though this

autonomous frequency exhibits slight variations through the locus curve. The computational cost is low, since modes at nearby frequencies are obtained simultaneously, such as those at 1.2 GHz and 1.6 GHz. As analyzed later, in this symmetric topology, the phase shift between the transistor stages may be different for the various oscillation modes, though all these modes are detected using a single small-signal current source I_s.

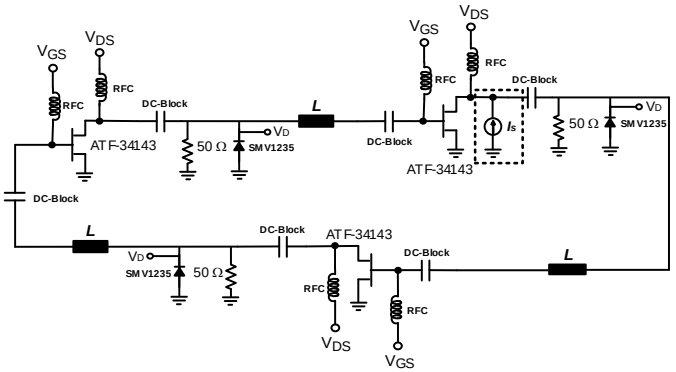

(a)

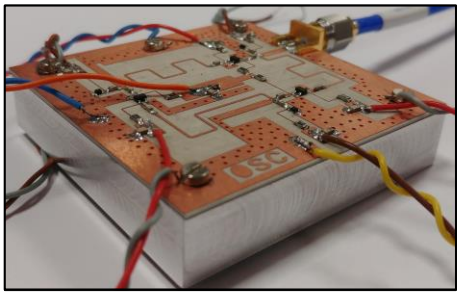

(b)

Fig. 4. Ring oscillator based on the transistor ATF-34143. (a) Schematic. Length of transmission line L = 40 mm. The small-signal current source I_s used for the detection of primary-Hopf bifurcations is indicated. The analysis of the periodic modes is carried out connecting an AG at the drain node of each of the three transistors. (b) Photograph of the manufactured prototype.

At low and high V_{GS}, the dc solution is stable for all the V_D values. As shown in Fig. 5(b), the primary Hopf loci corresponding to 2.6 GHz and 4.5 GHz exist for all the V_D values, and have nearly vertical left and right sections. The primary Hopf locus at 1.6 GHz is composed of two curves. One of the curves exists from V_D = 0 V to V_D = 2.14 V and the other one exists for V_D > 3.86 V. For V_D>4.93 V there is also a fourth primary-Hopf bifurcation locus at 1.2 GHz. Each Hopf locus has a left and right section where the corresponding pair of complex-conjugate poles cross to the RHS and to the LHS, respectively, when increasing V_{GS} from low value. The middle regions, comprised between all the direct and inverse Hopf locus sections, contain three pairs of complex-conjugate poles on the RHS for V_D<2.14 V, and four pairs of complex-conjugate poles on the RHS for V_D>4.96 V.

Due to the points with infinite slope of the locus curves and the fact that the oscillation frequencies detected in Fig. 5(a) are largely spaced, obtaining these loci with the usual bifurcation analysis methods [8], [27]-[28] would be cumbersome. The bifurcation condition $Y_s(V_D, V_{GS}, \omega) = 0$ should be solved through optimization under large variations of ω, in different ranges. Passing through each infinite-slope point requires a manual parameter switching, so one should initially sweep V_{GS}, solving $Y_s(V_D, \omega) = 0$, and then V_D, solving $Y_s(V_{GS}, \omega) = 0$.

Fig. 5(c) and Fig. 5(d) show the validation of the Hopf bifurcation loci through pole-zero identification [1]-[2], [18]. This has been carried out in two stages, initially using a coarse frequency sweep to detect the circuit resonances and then using a fine frequency sweep about each of the detected resonances. The results of these detailed pole-zero identifications have been assembled and are presented in Fig. 5(c) and Fig. 5(d).

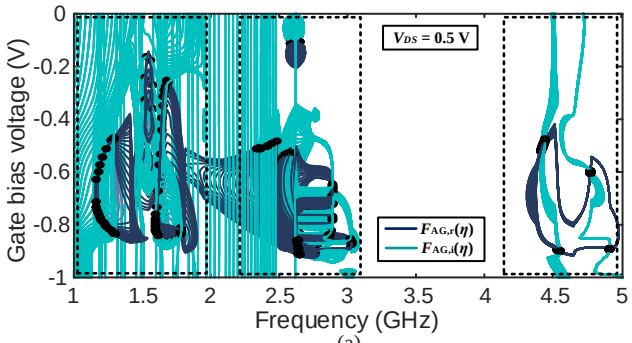

(a)

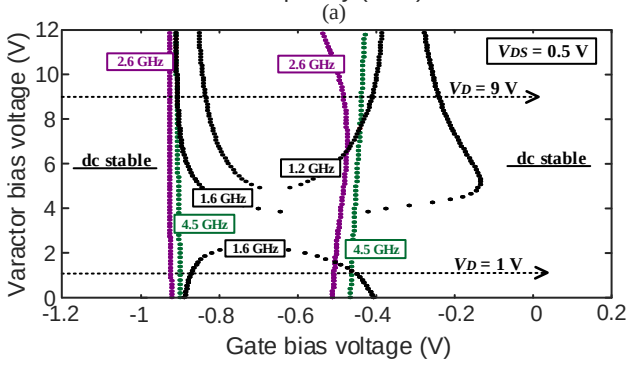

(b)

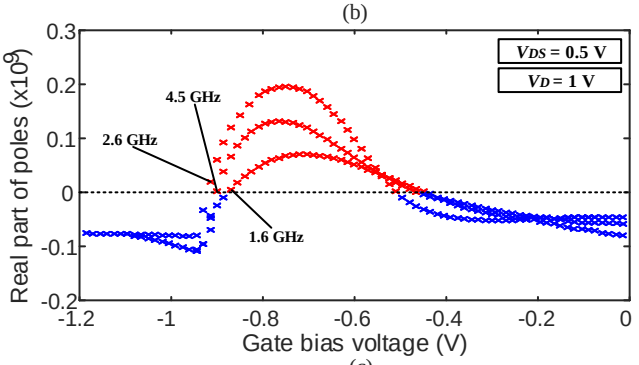

(c)

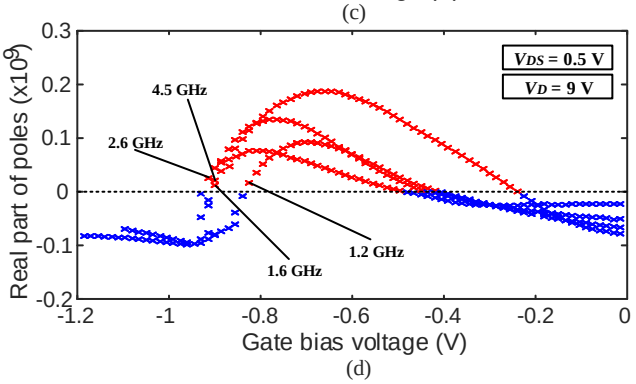

(d)

Fig. 5. Primary-Hopf bifurcation loci of the oscillator in Fig. 4 versus $\eta_1 = V_D$ and $\eta_2 = V_{GS}$. (a) Intersection points $[\omega_H(\eta_1),\eta_{2,H}(\eta_1)]$ obtained through a coarse frequency sweep. There are three clusters of solution points, about 1.6 GHz, 2.6 GHz and 4.5 GHz. (b) Bifurcation loci in the plane defined by V_{GS} and V_D. The oscillation frequency corresponding to each locus is marked. (c) Validation of the Hopf bifurcation loci through pole-zero identification for V_D = 1 V. (d) For V_D = 9 V.

In Fig. 5(c), a constant value V_D = 1 V has been considered, increasing V_{GS} from –1.2 V to 0 V. The real part of the dominant poles has been represented versus V_{GS}. When increasing V_{GS} from –1.2 V, the oscillator is initially stable. Then it undergoes a fast sequence of three direct Hopf bifurcations, so, in the interval V_{GS} = –0.86 V to V_{GS} = –0.5 V, the circuit exhibits three pairs of complex-conjugate poles on the RHS. At V_{GS} = –0.5 V the pair of poles at 2.6 GHz crosses to the LHS in an inverse Hopf bifurcation, which is followed by two other inverse Hopf bifurcations, at which the poles at 4.5 GHz and 1.6 GHz cross to the LHS. All the V_{GS} values at which the real part of the poles crosses through zero are accurately predicted by the primary Hopf loci in Fig. 5(b). This can be verified following the arrow corresponding to V_D = 1 V. Note that these loci provide the pairs (V_{GS}, V_D) at which the oscillator undergoes a primary Hopf bifurcation. In Fig. 5(d), a constant value V_D = 9 V has been considered, increasing V_{GS} from −1.2 V to 0 V. All the direct and inverse Hopf bifurcations are well predicted by the Hopf loci in Fig. 5(b), as can be verified by following the arrow corresponding to V_D = 9 V.

As will be shown in the next section, the solutions that are more likely to be observed experimentally are those arising from a stable dc regime or a dc regime with a small number of unstable poles [31]. This is because the unstable poles of the dc solution are transferred to the generated oscillatory periodic solution, in agreement with the well-known *bifurcation relationships* [22], [32]. Once in the oscillatory regime, and when varying the analysis parameter, these poles must cross to the LHS, in a series of inverse bifurcations, for the solution to become stable. Increasing V_{GS} from low value (following the arrow), the oscillation at 2.6 GHz arises from a stable dc regime. The rest of periodic solutions arise from a dc regime with one or more pairs of complex-conjugate poles on the RHS and are less likely to become stable. On the other hand, for V_D < 1.2 V and V_D > 3.86 V when decreasing V_{GS} from about 0 V, the oscillation that is generated from a stable dc regime is the one at 1.6 GHz. For V_D > 3.86 V, there is a high distance between the Hopf bifurcation at 1.6 GHz and the rest of bifurcations. Thus, one can expect the oscillations at 2.6 GHz and 1.6 GHz to be observed experimentally.

In summary, both Fig. 5(a) and Fig. 5(b) enable an exhaustive exploration of the oscillation modes under variations in two relevant parameters. To our knowledge, bifurcation loci of realistic multi-mode oscillators, with the complexity of those in Fig. 5(b), have never been obtained in any previous work. As shown in the following sections, these loci will be very useful for a reliable design of reconfigurable oscillators.

III. Calculation of Solution Curves

This section presents a methodology to obtain multivalued and possible multi-section periodic and quasi-periodic solution curves versus an arbitrary parameter η, in a systematic manner, without using continuation. The method is an extension of the one described in Section II. However, the admittance function Y_{AG} required to obtain the solution curves is *nonlinear* and must be extracted with a HB simulation, instead of a small-signal analysis. The extraction is carried out with an auxiliary generator [20], which is a voltage generator (playing the role of the oscillation) of amplitude A_{AG} and phase ϕ_{AG}, in series with an ideal bandpass filter at its operation frequency ω_{AG}. The AG is introduced in parallel at a sensitive circuit node [20], such as a device terminal.

In addition to the amplitude A_{AG}, a variable ξ_{AG} is considered, corresponding to the AG frequency, $\xi_{AG} = \omega_{AG}$, in an autonomous regime, or to the input-source phase, $\xi_{AG} = \phi_{in}$, in a forced regime (after setting the AG phase to zero, $\phi_{AG} = 0$). The Y_{AG} function is calculated through HB, as the ratio between the AG current and voltage. A triple sweep is performed in the analysis parameter η, ξ_{AG} and A_{AG}. When $\xi_{AG} = \phi_{in}$, the ξ_{AG} sweep is carried out between 0º and 360º. At each ξ_{AG} step, A_{AG} is swept from 0.01 to a few volts (depending on the transistor ratings). A HB simulation is carried out at each sweep step. The inner A_{AG} sweep allows taking advantage of the inherent continuation of the HB inner tier, using the last solution point as initial guess for the next point. One-tone HB is used in the case of a periodic regime and a two-tone HB is used in the case of an autonomous quasi-periodic regime, with a number of harmonic or intermodulation terms as high as required.

All the solution points $S(\eta)$ existing for η are exhaustively calculated from:

$$\begin{aligned} &Y^{\eta}_{AG,r}\left(\xi_{AG}, A_{AG}\right) = 0 \\ &Y^{\eta}_{AG,i}\left(\xi_{AG}, A_{AG}\right) = 0 \\ &S(\eta) = Y^{\eta}_{AG,r} \cap Y^{\eta}_{AG,i} \end{aligned} \tag{5}$$

The entire solution curve(s) are given by the whole set of intersection points $S(\eta)$ resulting from the η sweep.

A. Application to the multimode oscillator

In case of oscillation modes associated with circuit symmetries (as in the circuit of Fig. 4), the function Y_{AG} must be extracted using one AG per transistor stage, in order to sustain the oscillation through the whole structure. The AGs will be connected at equivalent nodes (e.g., at the gate or drain terminals) of the transistor stages. In the presence of circulant passive/active matrixes [34]-[37], the oscillation modes will have the same amplitude at equivalent circuit nodes and different phase shift $2\pi k/N$, where k = 1 to N−1 and N is the number of transistor stages. For each mode, the frequencies and amplitudes of the AGs will be the same [35]-[36], ω_{AG} and A_{AG}, and the phase shifts between the AGs will be sequentially fixed at $2\pi k/N$, where k = 1 to N−1. Then, the Y_{AG} function will be identical at all the transistor stages [34]-[36].

The new method has been applied to calculate the steady-state oscillations of the circuit in Fig. 4. This provides the solution curves in Fig. 6(a) and Fig. 6(c), traced with dots, in terms of V_{GS}, for constant varactor-bias voltage V_D = 1 V and V_D = 9 V, respectively. The voltage V_{GS} has been purposely used as parameter, instead of V_D, to obtain multivalued solution curves, as multivalued sections are commonly encountered about the conduction threshold [38]. In the two cases [Fig. 6(a) and Fig. 6(c)], the points at which the oscillation curves are originated and extinguished are consistent with the primary-Hopf bifurcations detected in Fig. 5. The distinct solution curves correspond to modes with different inter-stage phase shifts (0º and 120º), indicated in the figure. All the solution curves exhibit turning points or points of infinite slope, which have been obtained without continuation methods.

The accuracy of the systematic method has been validated comparing the curves in Fig. 6(a) and Fig. 6(c) with those obtained through AG optimization/parameter switching [20], superimposed in solid line. Results are overlapped, except in the upper section of the oscillation mode at 1.6 GHz in Fig. 6(a), where the curve exhibits a small loop (expanded view), virtually impossible to obtain through manual parameter switching.

For V_D = 1 V, and increasing V_{GS} from low value, the only mode arising from a stable dc solution is the one at 2.6 GHz. This is the only mode that could be observed experimentally, as well as other subharmonic and quasi-periodic solutions resulting from bifurcations of this mode. Measurement points of the mode at 2.6 GHz (before undergoing a frequency division by two, at the point indicated with "×") are shown in Fig. 6(a). This mode could be observed experimentally for V_{GS} between – 0.945 V and –0.96 V. Fig. 6(b) shows the output spectrum for V_{GS} = –0.95 V, with fundamental output power –6.2 dBm. None of the other oscillation modes detected in Fig. 5 could be observed experimentally, in consistency with the sequence of Hopf bifurcations from dc regime and the discussion at the end of *Section II.C*. For V_D = 9 V, and when decreasing V_{GS} from high value, the only mode arising from a stable dc solution is the one at 1.6 GHz, though in experiment there was a small frequency deviation [Fig. 6(d)]. We have verified that the spectrum in Fig. 6(d) is not due to a frequency division by two of the solution in Fig. 6(b). Actually, the fundamental frequency in Fig. 6(b) is 2.604 GHz, whereas the fundamental frequency in Fig. 6(d) is 1.4 GHz. Experimental points, corresponding to the 1.6 GHz mode, are superimposed in Fig. 6(c). By varying V_D and V_{GS} the circuit behaves as a dual-mode oscillator at 2.6 GHz and 1.4 GHz.

B. Application to a power amplifier

The method in equation (5) has been applied to obtain the oscillatory solution curves of the power amplifier in Fig. 1, versus the input power P_{in}. When varying P_{in}, both quasi-periodic solutions, at the input-source frequency ω_{in} and the autonomous oscillation frequency ω_a, and subharmonic solutions, at $\omega_{in}/2$, are obtained. To trace the quasiperiodic curves, the variable used in (5) is $\xi_{AG} = \omega_{AG}$ (playing the role of ω_a) and a two-tone HB simulation at ω_{in} and ω_{AG} must be performed.

The curves have been traced versus P_{in}, for V_{DS} = 1.5 V and three different values of V_{GS}. Results obtained for V_{GS} = –0.5 V are traced with dots in Fig. 7(a). For zero input power, the circuit exhibits a free-running oscillation, in consistency with the primary-Hopf locus in Fig. 2(b). When the input power is introduced, the mixing of ω_{in} with the oscillation frequency ω_a gives rise to an autonomous quasi-periodic regime. Increasing P_{in}, the quasi-periodic solution is extinguished at the inverse secondary Hopf bifurcation H [6]-[7], [20]. When further increasing P_{in}, a subharmonic curve arises at the flip bifurcation F [6]-[7], [20]. The subharmonic curve exhibits two turning points: TP_1 and TP_2. One of them (TP_1) is located at a small parameter distance from the quasi-periodic solution curve. No measurement points are superimposed since the represented oscillation amplitude corresponds to the drain voltage of one of the two transistors at ω_a and the odd multiples of the oscillation frequency are ideally cancelled at the output node. Their observation would only be due to discrepancies in the element values of the two amplifier branches. All the solution curves have been validated through AG optimization/parameter switching, with the results superimposed in solid line in Fig. 7(a).

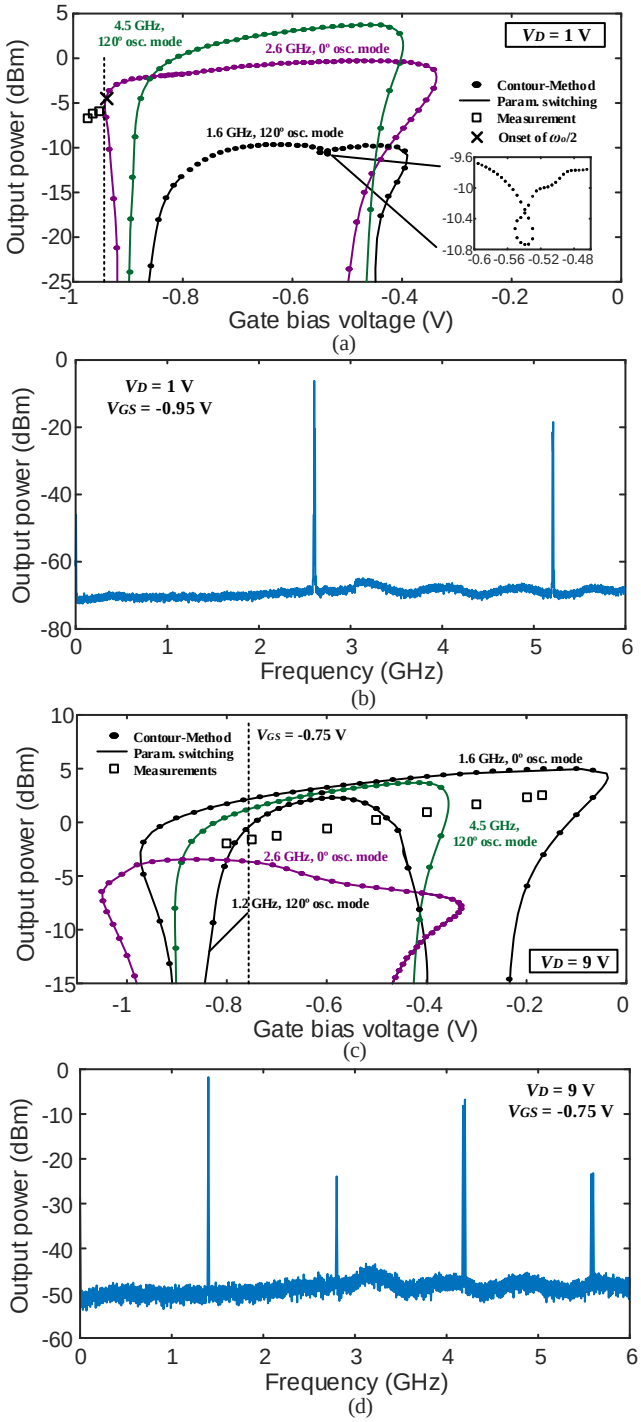

Fig. 6. Oscillation modes of the circuit in Fig. 4. (a) Solution curves traced in terms of V_{GS} for V_D = 1 V. The inter-stage phase shifts corresponding to the various oscillation modes are indicated. The results obtained with the new method (represented with dots) are compared with those obtained through AG optimization/parameter switching (in solid line). (b) Measured spectrum of the oscillation mode at 2.604 GHz for V_D = 1 V and V_{GS} = –0.95 V. (c) Solution

curves traced in terms of V_{GS} for V_D = 9 V. (d) Measured spectrum of the oscillation mode at 1.4 GHz for V_D = 9 V and V_{GS} = – 0.75 V.

Fig. 7(b) presents the output spectrum for P_{in} = 0 dBm, corresponding to an autonomous quasi-periodic solution, as predicted by the solution diagram of Fig. 7(a). Fig. 7(c) presents the output spectrum for P_{in} = 10 dBm, corresponding to a frequency division by 2, in consistency with Fig. 7(a). The analysis in Fig. 7(a) predicts an interval of stable periodic solutions at ω_{in} between the Hopf bifurcation H and the flip bifurcation F. However, these stable solutions could not be measured for this V_{GS} value. This should be due to the existence of turning points in the experimental quasi-periodic curves, giving rise to an overlapping of these quasi-periodic solutions with the stable periodic solution at ω_{in}. Those turning points could not be found in simulation for V_{GS} = –0.5 V, which is attributed to modelling inaccuracies. However, when changing the transistor gate-drain C_{gd} capacitance, as a small dispersion test, from 0.15 pF (nominal value) to 0.25 pF, turning points arise in the quasiperiodic curve [Fig. 7(d)], which would lead to jumps from quasiperiodic to subharmonic regime and vice versa.

For V_{GS} = –0.37 V and V_{GS} = –0.6 V one obtains the curves in Fig. 8(a), traced, respectively, with blue and red dots. For V_{GS} = –0.37 V, the turning point TP_2 of the subharmonic curve has vanished and this curve exhibits a loop before decaying to zero at the flip bifurcation F, as in the case of Fig. 7(d). In this case, there is a P_{in} interval for which the subharmonic curve does not coexist with the stable periodic solution at ω_{in} (comprised between H and F). This situation, which is not found for V_{GS} = –0.5 V and V_{GS} = –0.6 V, should facilitate the experimental observation of this periodic solution. See the output spectrum obtained for P_{in} = 18 dBm in Fig. 8(b). For V_{GS} = –0.6 V, the subharmonic solution is composed by two disconnected curves, which would be difficult to detect with an ordinary method. In view of this result, one can suspect that bifurcation diagrams obtained through continuation will often miss curve sections. Note that there is no way to predict the frequency division in the closed curve through a stability analysis of the periodic regime at ω_{in}. After its detection with the new methodology, this solution curve has also been obtained through AG optimization and parameter switching (in solid line).

It can be of interest to compare the advantages and drawbacks of the new method (M_1) and the one based on AG optimization/parameter switching (M_2). When tracing a non-problematic curve section, the computation time of M_2 is shorter, since it directly addresses each solution point, whereas M_1 is based on the extraction of the nonlinear function $Y_{AG}^{\eta}(\xi_{AG}, A_{AG})$. However, M_2 demands user surveillance and manual parameter switching, so the total time devoted to the circuit simulation may be very long in complex solution curves. Furthermore, there can be situations in which no convergence is obtained with M_2. This is because the two-tier representation (where Y_{AG} = 0 is the outer tier and the pure HB system the inner tier) limits the parameter switching to only three variables, though the nonlinear circuit is actually governed by a HB system with many more state variables. These convergence failures leave the user without any possibility to complete the solution curves. In addition, M_2 is not exhaustive, unlike M_1, so it will miss isolated curves, like the one in Fig. 8(a).

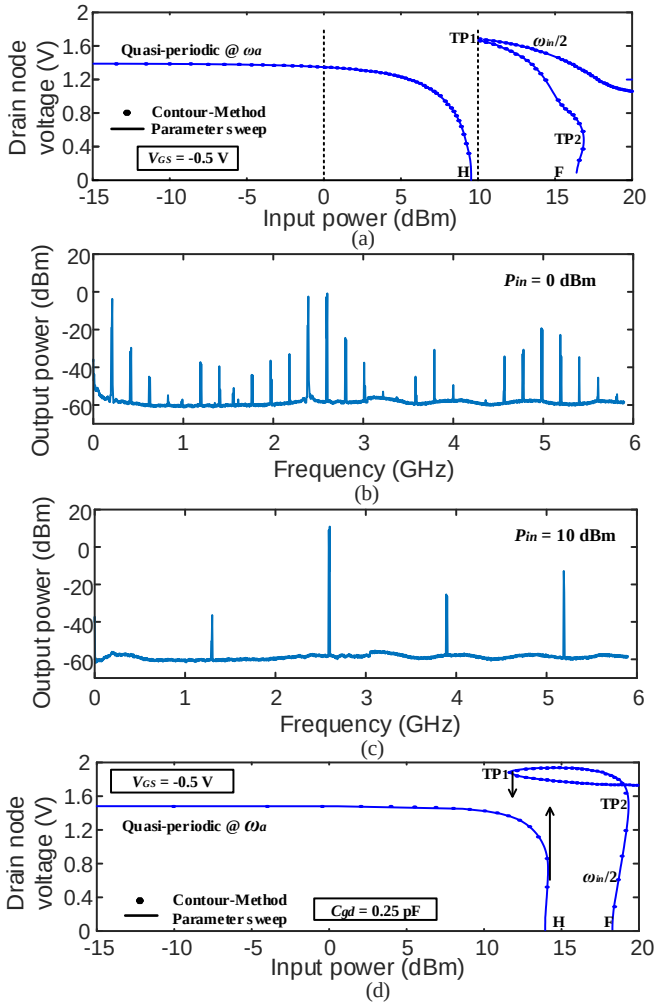

Fig. 7. Power amplifier. (a) Quasiperiodic and subharmonic solution curves, traced in terms of the drain voltage at $f_a = \omega_a/2\pi \cong 1.32$ GHz and $f_{in}/2$ = 1.5 GHz, respectively, versus P_{in}, for V_{DS} = 1.5 V and V_{GS} = –0.5 V. Curves obtained with the new method are traced with dots. Curves obtained with AG optimization/parameter switching are superimposed in solid line. (b) Measured spectrum at P_{in} = 0 dBm. (c) Measured spectrum at P_{in} = 10 dBm. (d) Small dispersion test, by changing C_{gd} from 0.15 pF (nominal value) to 0.25 pF.

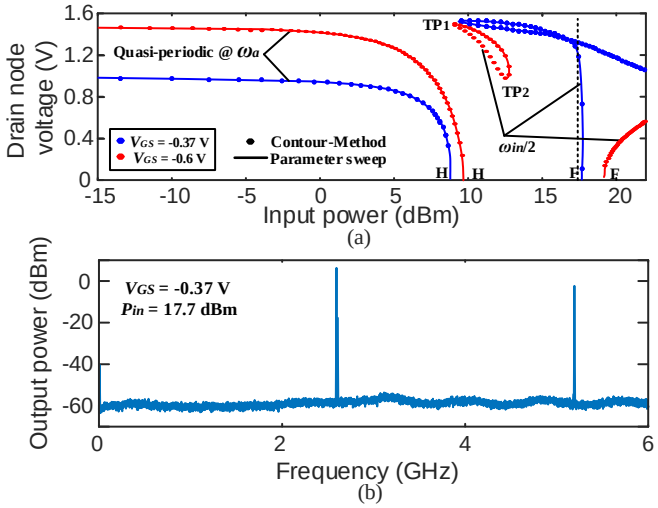

Fig. 8. Power amplifier. (a) Subharmonic and quasiperiodic solution curves in terms of the drain voltage at $f_a = \omega_a/2\pi = 1.32$ GHz and $f_{in}/2 = 1.5$ GHz, respectively, versus P_{in} for $V_{DS} = 1.5$ V and two gate-bias voltages: $V_{GS} = -0.37$ V (blue) and $V_{GS} = -0.6$ V (red). Curves obtained with the new method are traced with dots. Curves obtained through AG optimization/parameter switching are traced with solid line. (b) Measured spectrum for $P_{in} = 18$ dBm and $V_{GS} = -0.37$ V.

IV. Bifurcation loci from periodic regime

The three types of local bifurcations from periodic regime are flip, Hopf and turning-point bifurcations [6]-[10]. At flip and Hopf bifurcations an oscillation is generated/extinguished with zero amplitude. At turning-point bifurcations, the solution curve exhibits an infinite slope. The exhaustive calculation of the corresponding bifurcation loci in a two-parameter space (η_1, η_2) is presented in the following paragraphs.

A. Hopf and flip bifurcations

At a Hopf bifurcation from a periodic regime at ω_{in}, a pair of complex-conjugate poles $\sigma \pm j\omega_a$, where ω_a is incommensurable with ω_{in}, crosses the imaginary axis of the complex plane, giving rise to the generation or extinction of a quasi-periodic regime [6]-[10]. On the other hand, at a flip bifurcation from a periodic solution at ω_{in} [6]-[10], a pair of complex-conjugate poles $\sigma \pm j\omega_{in}/2$ crosses the imaginary axis of the complex plane, giving rise to the generation/extinction of a subharmonic oscillation at $\omega_{in}/2$.

The Hopf (flip) bifurcations can be detected introducing a small-signal AG at ω_a ($\omega_{in}/2$) into the circuit. Note that the circuit operates in large-signal conditions with respect to the input source at ω_{in} but in small signal with respect to the AG, since its amplitude is set to a small value. This AG will be used to obtain the small-signal admittance Y_{AG}, which should be zero at both the Hopf and flip bifurcations.

For each η_1, a double sweep is performed in ξ_{AG} and η_2, where $\xi_{AG} = \omega_a$, for the Hopf-bifurcation detection, and $\xi_{AG} = \phi_{in}$, for the flip-bifurcation detection. The double sweep in ξ_{AG} and η_2 has a very low computational cost due to the small-signal amplitude of the AG. All the bifurcation points $B(\eta_1)$ existing for η_1 are exhaustively calculated from:

$$\begin{aligned} &Y_{AG,r}^{\eta_1}(\xi_{AG}, \eta_2) = 0 \\ &Y_{AG,i}^{\eta_1}(\xi_{AG}, \eta_2) = 0 \\ &B(\eta_1) = Y_{AG,r}^{\eta_1} \cap Y_{AG,i}^{\eta_1} \end{aligned} \tag{6}$$

The entire bifurcation curve(s) are given by the whole set of intersection points $B(\eta_1)$ resulting from the η_1 sweep.

B. Turning points

At a turning point bifurcation, obtained when varying a parameter η, two points of a same solution curve (S_1 and S_2) merge and annihilate, which gives rise to an infinite slope. The bifurcation relationship, in a ball of the state-variable space, with radius tending to zero, can be expressed as [6], [22]:

$$S_1^n + S_2^{n+1} \rightleftarrows \varnothing \tag{7}$$

where the superscript indicates the number of unstable canonical poles and the symbol $\varnothing$ indicates no solutions. Since a real pole passes through zero at the turning point bifurcation, the difference between the number of unstable poles of S_2 and S_1 is necessarily $\Delta n = 1$. The relationship (7) is fulfilled at turning points in solution curves of any kind of regime, i.e. dc, periodic or quasi-periodic.

When using the new geometrical method to obtain solution curves, the turning points can easily be detected in the following manner. One should keep track of the number of steady-state solutions obtained for each parameter value $\eta(k)$, expressed as $m[\eta(k)]$, where k is a counter of the parameter values for which solutions are found. Taking (7) into account, turning points are obtained at the η values where m increases or decreases in 2. Thus, at a turning-point, the following condition is fulfilled:

$$m[\eta(k)] - m[\eta(k+1)] = \pm 2 \tag{8}$$

The above condition enables a straightforward calculation of the turning-point locus, as shown later in this section. Additionally, at the design stage, one can predict the occurrence of turning points by evaluating the Jacobian matrix of the outer-tier admittance function Y_{AG} with respect to A_{AG} and ξ_{AG}. As demonstrated in [21], this Jacobian matrix becomes singular at turning points, which fulfill:

$$\det(Y_{AG}) = \frac{\partial Y_{AG,r}}{\partial A_{AG}} \frac{\partial Y_{AG,i}}{\partial \xi_{AG}} - \frac{\partial Y_{AG,r}}{\partial \xi_{AG}} \frac{\partial Y_{AG,i}}{\partial A_{AG}} = 0 \tag{9}$$

By continuity, the function $\det(Y_{AG})$ will have opposite sign at the two points that arise or annihilate at the turning point (just before or after this bifurcation). The determinant $\det(Y_{AG})$ is easily calculated through a spline interpolation of $Y_{AG,r}^{\eta_1}$ and $Y_{AG,i}^{\eta_1}$, plus application of gradient operators. If the solution points with a positive determinant $m^P[\eta(k)]$ and negative determinant $m^N[\eta(k)]$ are counted, an additional condition for turning point is:

$$m^P[\eta(k)] - m^P[\eta(k+1)] = m^N[\eta(k)] - m^N[\eta(k+1)] = \pm 1 \tag{10}$$

The ±1 is due to the fact that the determinant has opposite sign at the two steady-state solutions that appear/disappear at the turning point. Thus, both the number of solutions with $\det(Y_{AG})>0$ (m^P) and the number of solutions with $\det(Y_{AG})<0$ (m^N) must increase or decrease in one.

The new procedure for the calculation of turning points will be illustrated through its application to the closed subharmonic-solution curve in Fig. 8(a), at $V_{GS} = -0.6$ V. For each parameter value $\eta = P_{in}$, the function $\det(Y_{AG})$ has been evaluated at all the interpolated points ϕ_{in}, A_{AG}, which has enabled the calculation of the contour $\det(Y_{AG}) = 0$, represented in Fig. 9 in the plane defined by ϕ_{in} and A_{AG}, the latter agreeing with the amplitude of the first-harmonic of the drain-node voltage. This contour changes with the parameter η, which is emphasized through the notation $\det^{\eta}(\phi_{in}, A_{AG})$.

When varying $\eta = P_{in}$, one obtains the set of solution points (indicated with circles) and contours $\det^{\eta}(\phi_{in}, A_{AG}) = 0$ (traced in solid line), shown in Fig. 9. The number between the braces in "$\eta()$" is a counter of the parameter values for which steady-state solutions are encountered. For each $\eta = P_{in}$, the contour $\det^{\eta}(\phi_{in}, A_{AG}) = 0$ constitutes the boundary between the ϕ_{in}, A_{AG} values providing $\det(Y_{AG}) > 0$ and $\det(Y_{AG}) < 0$. The turning-point bifurcations must fulfill both $(Y_{AG,r}^{\eta} = 0) \cap (Y_{AG,i}^{\eta} = 0)$ and

$\det^{\eta}(\phi_{in},A_{AG}) = 0$, which in the case of Fig. 8(a) and Fig. 9 occurs only for two ϕ_{in},A_{AG} values: ϕ_{in} = 179° and A_{AG} = 1.504 V, ϕ_{in} = 192° and A_{AG} = 1.49 V.

Note that obtaining the contour $\det^{\eta}(\phi_{in},A_{AG}) = 0$ is not necessary for the evaluation of the turning-point conditions (8) and (10). However, its calculation has very low computational cost and can enable an early detection and suppression of turning points during the design procedure, in a similar manner to what was done in Fig. 2(d) with the stabilization resistor.

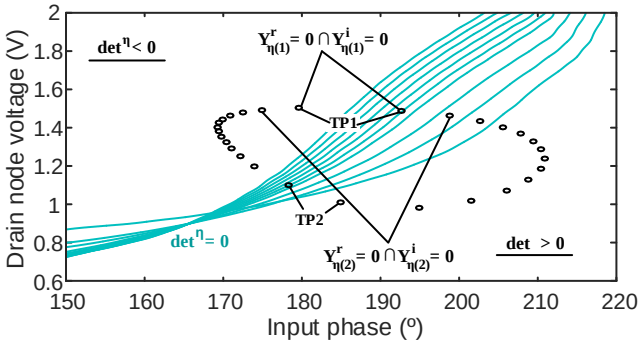

Fig. 9. Subharmonic solutions of the power amplifier in the plane defined by ϕ_{in} and the amplitude at the drain node (agreeing with A_{AG}) for V_{GS} = –0.6 V. The input power has been swept between 9 dBm and 13 dBm. The solution points obtained in this interval are traced with circles. The contours $\det^{\eta}(\phi_{in},A_{AG}) = 0$ are traced in solid line.

Conditions (8) are easily extended to an analysis in terms of two parameters η_1, η_2. This is done by performing two nested sweeps, in η_1, η_2. At each step of the outer sweep in η_1, one stores all the η_2 points, denoted as η_{2T}, that fulfill (8). The turning point locus is obtained by representing η_{2T} versus η_1.

C. Application to a power amplifier

The bifurcation-analysis method has been applied to the power amplifier in Fig. 1. The bifurcation loci have been calculated in terms of $\eta_1 = V_{GS}$ and $\eta_2 = P_{in}$ for two values of the drain-bias voltage: V_{DS} = 1.5 V, in Fig. 10(a), and V_{DS} = 3 V, in Fig. 10(b). These two values have been selected since, as shown later, they give rise to qualitatively different bifurcation loci in the plane (V_{GS}, P_{in}).

For V_{DS} = 1.5 V one obtains a flip locus composed of two disconnected curves (Flip Locus 1 and Flip Locus 2) that cannot be easily detected using ordinary techniques. When V_{GS} is swept from –0.7 V to –0.3 V, the new method simultaneously provides points in the two flip-locus curves. This is shown in Fig. 12(a), which presents the intersections between $Y^{\eta_1}_{AG,r}(\phi_{in},\eta_2) = 0$ and $Y^{\eta_1}_{AG,i}(\phi_{in},\eta_2) = 0$, obtained in the η_1 interval comprised between V_{GS} = –0.67 V and V_{GS} = – 0.63 V. The lower (upper) intersection points correspond to Flip Locus 1 (Flip Locus 2). Each family of intersection points correspond to one of the two loci.

The versatility of the new method enables an investigation of the effect of an additional (third) parameter on the locus curves. In Fig. 12(b), V_{DS} has been added as a third parameter. Increasing V_{DS}, the two disconnected flip locus curves approach each other and merge into a single one. To our knowledge, no analysis of such complexity has ever been performed in combination with HB commercial software. At V_{DS} = 1.5 V and V_{DS} = 3 V, one respectively obtains two flip loci and one flip locus, leading to a qualitatively different behavior. This is why these V_{DS} values have been chosen in this investigation.

As shown in Fig. 10(a), the Flip Locus 1 exhibits a pronounced minimum at V_{GS} = –0.88 V because for that V_{GS} value the frequency of the (stable) dominant complex-conjugate poles approaches the input frequency divided by two. The Hopf locus only exists on the right side of the flip locus. The Hopf-locus point corresponding to P_{in} = –∞ dBm (in the absence of input power) agrees with the primary-Hopf bifurcation obtained in the analysis of Fig. 2 for V_{GS} = –0.83 V and V_{DS} = 1.5 V. The Hopf and flip loci merge at the two co-dimension two bifurcations [12]-[13] indicated in the figure as CT_1 and CT_2. The periodic solution at the input-drive frequency ω_{in} is unstable inside the flip locus and inside the Hopf locus.

To complete the stability portrait, the locus of turning points in subharmonic regime has also been represented in the plane (V_{GS}, P_{in}) [see Fig. 10(a)]. Performing a double sweep in V_{GS} and P_{in}, one obtains two turning-point locus sections, shown in Fig. 10(a), respectively denoted as TP_1 Locus and TP_2 Locus. In fact, the turning points observed in the subharmonic solution curves of Fig. 7 and Fig. 8 (also denoted as TP_1 and TP_2) belong to these two sections. Closed subharmonic solution curves [such as the one in Fig. 8(a)] are obtained in the region of the plane in Fig. 10(a) located between the two sections of the flip locus. After the intersection of the TP2 Locus and the Flip Locus 2 one obtains open subharmonic curves, as the one in Fig. 7(a).

Turning-point bifurcations may correspond to two different phenomena: jumps and synchronization [20]-[21]. When departing from a quasi-periodic solution and varying any of the two analysis parameters in its full range, synchronization points will be those traversed without ever crossing the Hopf locus. This is because synchronization is the only mechanism for the quasi-periodic solution to transform into a subharmonic one. When also traversing the Hopf locus, synchronization points may still exist but their identification is demanding, since it requires the detection of the global saddle-connection bifurcation [12], [20], [31]. The size of the parameter intervals for which this bifurcation occurs is typically very small and located near the co-dimension two bifurcations. Thus, this bifurcation is not generally very relevant.

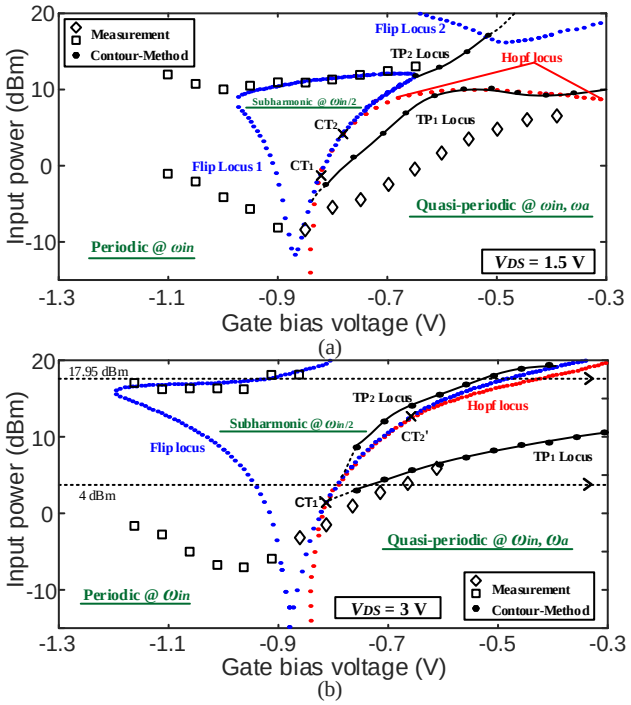

Fig. 10. Flip and Hopf and turning-point loci of the power amplifier, traced in terms of $\eta_1 = V_{GS}$ and $\eta_2 = P_{in}$. The periodic solution at $f_{in} = 3$ GHz is unstable inside the flip locus and inside the Hopf locus. (a) $V_{DS} = 1.5$ V, with two disconnected flip-locus sections. (b) $V_{DS} = 3$ V, with a single flip locus.

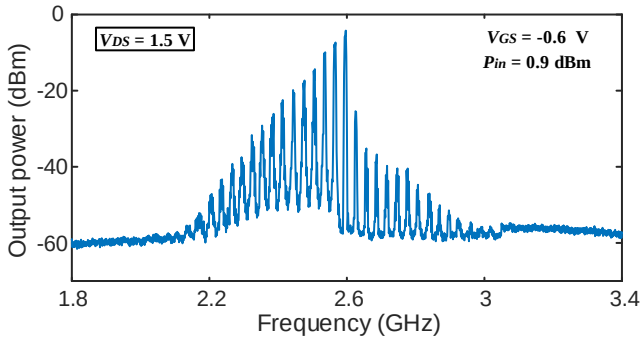

Fig. 11. Measured spectrum at the transition between quasi-periodic and subharmonic regime.

From the previous discussion, one can assure that turning points obtained for P_{in} values between CT_1 and CT_2 will be synchronization points. However this interval will actually be broader. Due to the occurrence of this synchronization phenomenon, subharmonic solutions exist for P_{in} values smaller than the one at which the flip bifurcation takes place.

Measurement points at the boundary between the parameter regions with stable behavior at ω_{in} and subharmonic behavior at $\omega_{in}/2$ are superimposed with squares in Fig. 10(a). For V_{GS} values on the right side of the Hopf locus, as P_{in} increases from low value, one initially observes a quasiperiodic spectrum and then a frequency-division by two. The experimental points where the transitions occur are represented with diamonds. At these transitions, a triangular spectrum, characteristic of synchronization, is observed (Fig. 11), which is in agreement with the presence of the turning-point locus of Fig. 10(a).

As shown in Fig. 10 there is good qualitative agreement between simulation and measurements. Discrepancies are due to the different shape of the experimental loci, which is attributed modelling inaccuracies. In the next subsection, the bifurcation loci will be validated through pole-zero identification, which is an independent analysis method, relying on identical models of the circuit components. Thus, there should be a perfect correspondence between the two methods.

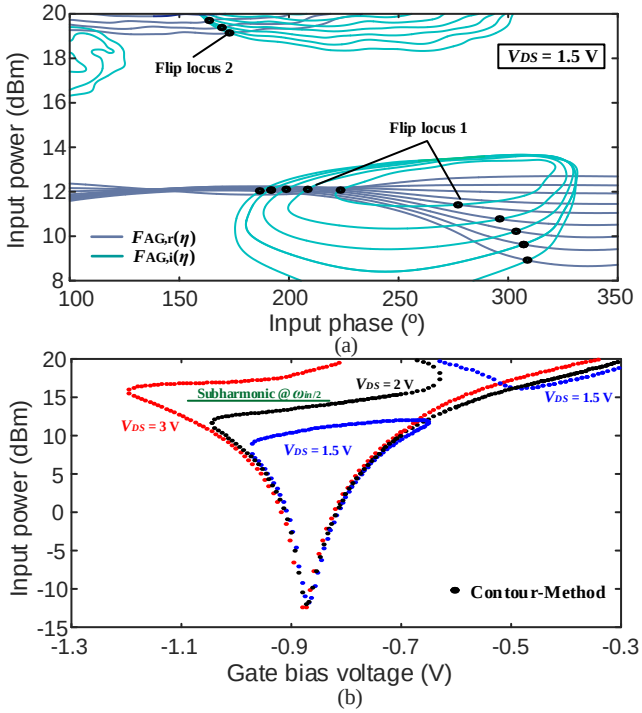

Fig. 12. Flip bifurcations of the power amplifier in Fig. 1 for $V_{DS} = 1.5$ V. (a) Simultaneous calculation of flip-bifurcation points in Flip Locus 1 and Flip Locus 2 of Fig. 9(a). The figure presents the intersections between $Y^{\eta_1}_{AG,r}(\phi_{in},\eta_2)=0$ and $Y^{\eta_1}_{AG,i}(\phi_{in},\eta_2)=0$, obtained for $V_{DS} = 1.5$ V in the η_1 interval comprised between $V_{GS} = -0.67$ V and $V_{GS} = -0.63$ V. (b) Investigation of the effect of V_{DS} on the flip-locus curve(s).

D. Validation with pole-zero identification

The predictions by the flip and Hopf loci have been validated through pole-zero identification. In Fig. 13, the real part of dominant poles obtained for $V_{DS} = 3$ V and two input-power values, $P_{in} = 4$ dBm and $P_{in} = 17.95$ dBm, has been represented versus V_{GS}. For $P_{in} = 4$ dBm [Fig. 13(a)] and low V_{GS}, the circuit is initially stable, as expected with the transistor below conduction. There is a stable pair of dominant complex-conjugate poles $\sigma \pm j\omega_a$, where $\omega_a/(2\pi) \cong 1.4$ GHz. When varying the parameter, ω_a will vary continuously. Increasing V_{GS}, the pair of poles at $\sigma \pm j\omega_a$ transforms into two distinct pairs of complex-conjugate poles at $\omega_{in}/2$ at $V_{GS} = -0.98$ V. These two distinct pairs of poles are denoted as $\sigma \pm j\omega_{in}/2$ and $\sigma' \pm j\omega_{in}/2$. The pair of poles $\sigma \pm j\omega_{in}/2$ crosses to the RHS at $V_{GS} = -0.94$ V, in a direct flip bifurcation (F_1), from which the periodic solution at ω_{in} becomes unstable. This flip bifurcation is consistent with the prediction by the flip locus in Fig. 10(b), as verified by following the arrow at $P_{in} = 4$ dBm, indicating the V_{GS} variation. Every crossing of the arrow through the flip locus corresponds to a flip bifurcation, at which the pair of poles $\sigma \pm j\omega_{in}/2$ crosses the imaginary axis. At $V_{GS} = -0.79$ V the same pair of poles $\sigma \pm j\omega_{in}/2$ crosses to the LHS in an inverse flip bifurcation (F_2) that is also accurately predicted by the locus

in Fig. 10(b). Just after crossing (V_{GS} = –0.77 V), the two pairs of unstable complex-conjugate poles $\sigma \pm j\omega_{in}/2$ and $\sigma' \pm j\omega_{in}/2$ merge into a pair of complex-conjugate poles $\sigma \pm j\omega_a$ and cross to the RHS in a Hopf bifurcation (H). This Hopf bifurcation is also consistent with the prediction by the Hopf locus in Fig. 10(b), as verified by further following the arrow corresponding to P_{in} = 4 dBm, as V_{GS} increases. The crossing of the arrow through the Hopf locus indicates a Hopf bifurcation, at which the pair of poles $\sigma \pm j\omega_a$ crosses the imaginary axis. There is only a small V_{GS} interval with stable behavior, in consistency with the neighborhood to the co-dimension two bifurcation CT_1' predicted by the loci in Fig. 10(b).

For P_{in} = 17.95 dBm [Fig. 13(b)] and low V_{GS}, the circuit is initially stable. There is a flip bifurcation at V_{GS} = –0.88 V (F_1), where a pair of complex-conjugate poles $\sigma \pm j\omega_{in}/2$ crosses to the RHS. At V_{GS} = –0.45 V , this same pair of poles crosses the imaginary axis to the LHS, in an inverse flip bifurcation (F_2) that is also consistent with the prediction of the locus in Fig. 10(b), when following the arrow corresponding to P_{in} = 17.95 dBm. Just after crossing (V_{GS} = – 0.445 V), the stable pair of poles $\sigma \pm j\omega_{in}/2$ merges the second stable pair $\sigma' \pm j\omega_{in}/2$ and they become a pair of complex-conjugate poles at an incommensurable frequency, $\sigma \pm j\omega_a$, which crosses to the RHS at V_{GS} = –0.39 V in a direct Hopf bifurcation (H). Note the consistency between the results of the two methods (by following the arrow corresponding to P_{in} = 17.95 dBm), even though the bifurcations are closely spaced. Identical consistency has been found in all the additional validations performed by varying the input power and biasing conditions.

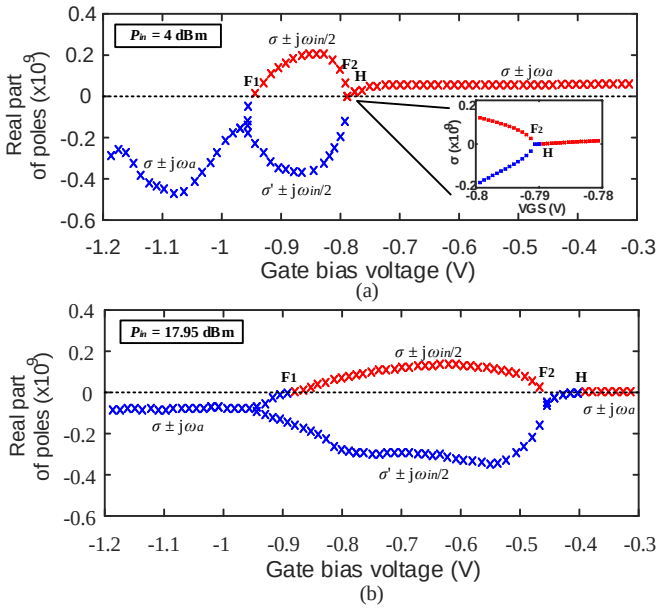

Fig. 13. Validation of the flip and Hopf bifurcation loci versus V_{GS} in Fig. 10(b) through pole-zero identification. (a) P_{in} = 4 dBm. (b) P_{in} = 17.95 dBm.

V. Conclusion

A conceptually simple methodology for an exhaustive bifurcation analysis in nonlinear circuits, which does not rely on continuation techniques, has been presented. Its main advantages are its systematic quality and its global exploration capabilities. When tracing the bifurcation loci, the method simultaneously provides bifurcation points corresponding to different locus sections and even disconnected locus curves. The method is intended for application in combination with commercial harmonic-balance software, from which an admittance function, depending on the analysis parameters, is extracted. It enables an efficient calculation of instability boundaries in nonlinear circuits prone to instability, such as power amplifiers. It also allows a systematic investigation of the complex problem of multiple oscillation modes in multi-device oscillators and oscillators loaded with multi-resonant networks. The calculation of the turning point locus has a high computational complexity with ordinary methods, which impose a singularity condition to the nonlinear-system Jacobian matrix. Here it is obtained in an original manner, taking into account the annihilation of solution points occurring at this type of bifurcation. The new method has been successfully validated through its application to a power amplifier and a multi-mode symmetric oscillator.

Acknowledgment

Authors would like to acknowledge Jesus de Cos from Erzia Technologies and Mabel Pontón and Sergio Sancho from Universtiy of Cantabria for helpful discussions.

References

[1] J. Jugo, J. Portilla, A. Anakabe, A. Suárez, and J. M. Collantes, "Closed-loop stability analysis of microwave amplifiers," *IEEE Electronics Letters*, vol. 37, no. 4, pp. 226–228, Feb. 2001.

[2] A. Anakabe, J. M. Collantes, J. Portilla, et al. "Analysis and elimination of parametric oscillations in monolithic power amplifiers," *2002 IEEE MTT-S Int. Microwave Symp. Dig.*, Seattle, WA, Jun. 2002, pp. 2181–2184.

[3] S. Mons, J.-C. Nallatamby, R. Queré, P. Savary, and J. Obregon, "A unified approach for the linear and nonlinear stability analysis of microwave circuits using commercially available tools," *IEEE Trans. Microw. Theory Techn.*, vol. 47, no. 12, pp. 2403–2409, Dec. 1999.

[4] S. Jeon, A. Suárez, R. Rutledge, "Global stability analysis and stabilization of a Class-E/F amplifier with a distributed active transformer," *IEEE Trans. Microw. Theory Techn.*, vol. 53, no. 12, Dec. 2005, pp. 3712–3722.

[5] S. Jeon, A. Suárez, R. Rutledge, "Analysis and elimination of hysteresis and noisy precursors in power amplifiers," *IEEE Trans. Microw. Theory Techn.*, vol. 54, no. 3, pp. 1096–1106, Mar. 2006.

[6] V. Rizzoli and A. Neri, "State of the art and present trends in nonlinear microwave CAD techniques," *IEEE Trans. Microw. Theory Techn.*, vol. 36, no. 2, pp. 343–356, Feb., 1988.

[7] R. Quéré, E. Ngoya, M. Camiade, A. Suarez, M. Hessane and J. Obregon, "Large signal design of broadband monolithic microwave frequency dividers and phase-locked oscillators," *IEEE Trans. Microw. Theory Techn.*, vol. 41, no. 11, pp. 1928–1938, Nov., 1993.

[8] A. Suárez, R. Quéré, *Stability Analysis of Nonlinear Microwave Circuits*. Artech House, Norwood (Ma), Jan. 2003.

[9] A. Suárez, "Radiofrequency stability analysis", Wiley Encyclopedia of Electrical and Electronics Engineering, Oct. 2012.

[10] V. Rizzoli, A. Lipparini, "General stability analysis of periodic steady-state regimes in nonlinear microwave circuits," *IEEE Trans. Microw. Theory Techn.*, vol. 33, no. 1, pp. 30 – 37, Jan. 1985.

[11] T.S. Parker, L.O. Chua, *Practical Numerical Algorithms for Chaotic Systems*, Springer-Verlag, New York, 1989.

[12] J. Guckenheimer and P. Holmes, *Nonlinear Oscillations, Dynamical Systems and Bifurcations of Vector Fields*. New York: Springer-Verlag, 1990.

[13] S. Wiggins, *Introduction to Applied Nonlinear Dynamical Systems and Chaos*. New York: Springer-Verlag, 1990.

[14] G. Ioos, D. Joseph, *Elementary Stability and Bifurcation Theory*. New York. Springer, 1980.

[15] J. M. T. Thompson and H. B. Stewart, *Nonlinear dynamics and chaos*, Second Edition, Wiley, 2002.
[16] A. Platzker, W. Struble, "Rigorous determination of the stability of linear n-node circuits from network determinants and the appropriate role of the stability factor K of their reduced two-ports," in Third International Workshop on Integrated Nonlinear Microwave and Millimeterwave Circuits, pp. 93–107, 5–7, Oct. 1994.
[17] W. Struble, A. Platzker, "A rigorous yet simple method for determining stability of linear N-port networks [and MMIC application]," in 15th Gallium Arsenide Integrated Circuit (GaAs IC) Symposium, pp. 251 – 254, 1993.
[18] N. Ayllon, J. M. Collantes, A. Anakabe, I. Lizarraga, S. Soubercaze-Pun, S. Forestier, "Systematic approach to the stabilization of multitransistor circuits", *IEEE Trans. Microw. Theory Techn.*, vol. 59, no. 8, pp. 2073–2082, Aug. 2011.
[19] J. M. Collantes, I. Lizarraga, A. Anakabe, J. Jugo, "Stability verification of microwave circuits through Floquet multiplier analysis," *2004 IEEE APCCAS*, Taiwan, 2004, pp. 997–1000.
[20] A. Suárez, *Analysis and Design of Autonomous Microwave Circuits*. IEEE-Wiley, Hoboken, (NJ) Jan. 2009.
[21] A. Suárez, J. Morales, R. Quéré, "Synchronization analysis of autonomous microwave circuits using new global-stability analysis tools," *IEEE Trans. Microw. Theory Techn.*, vol. 46, no. 5, pp. 494–504, May 1998.
[22] H. Kawakami, "Bifurcation of periodic responses in forced dynamic nonlinear circuits: Computation of bifurcation values of the system parameters," *IEEE Transactions on Circuits and Systems*, vol. 31, no. 3, pp. 248-260, Mar 1984.
[23] J. de Cos and A. Suárez, "Efficient Simulation of Solution Curves and Bifurcation Loci in Injection-Locked Oscillators," *IEEE Trans. Microw. Theory Techn.*, vol. 63, no. 1, pp. 181-197, Jan. 2015.
[24] J. de Cos, A. Suárez and J. A. García, "Hysteresis and Oscillation in High-Efficiency Power Amplifiers," *IEEE Trans. Microw. Theory Techn.*, vol. 63, no. 12, pp. 4284-4296, Dec. 2015.
[25] E. Palazuelos, A. Suárez, J. Portilla, J. Barahona "Hysteresis prediction in autonomous microwave circuits using commercial software. Application to a Ku band MMIC VCO," *IEEE Journal of Solid-State Circuits*, vol. 33, no. 8, Aug. 1998, pp.1239-1243.
[26] A. Goel and H. Hashemi, "Frequency Switching in Dual-Resonance Oscillators," *IEEE Journal of Solid-State Circuits*, vol. 42, no. 3, pp. 571-582, March, 2007.
[27] F. Ramírez, A. Suárez, S. Sancho, "Oscillation Modes in Free-Running Oscillators Loaded with Multi-Resonant Networks," *2016 IEEE MTT-S Int. Microwave Symp.*, San Francisco, CA, USA, May, 2016.
[28] F. Ramírez, S. Sancho, A. Suárez, "Oscillation Modes in Free-Running Oscillators Loaded with Multi-Resonant Networks," *IEEE Trans. Microw. Theory Techn.*, vol. 64, no. 12, pp. 1-16, Dec., 2016.
[29] A. Ballato, "Piezoelectric Resonators," in B. Parzen, Design of Crystal and Other Harmonic Oscillators, pp. 66-122, John Wiley and Sons, 1983.
[30] S. Hernández, M. Pontón and A. Suárez, "Simulation Method for Complex Multivalued Curves in Injection-Locked Oscillators," *IEEE Trans. Microw. Theory Techn.*, vol. 65, no. 11, pp. 4046-4062, Nov. 2017.
[31] J. de Cos and A. Suárez, "Stability Analysis of Injection-Locked Multimode Oscillators," *IEEE Trans. Microw. Theory Techn.*, vol. 61, no. 8, pp. 2878-2891, Aug. 2013.
[32] N. V. Butenin, Y. I. Neimark, and N. A. Fufaev, *Introduction to the Theory of Non-Linear Oscillations (in Spanish)*. Moscow, Russia: Mir, 1991.
[33] S. Ver Hoeye, L. Zurdo, A. Suárez, "New nonlinear design tools for self-oscillating mixers", *IEEE Microwave and Wireless Components Letters*, vol. 11, no. 8, pp.337-339, Aug. 2001.
[34] K. Kurokawa, "An analysis of Rucker's multidevice symmetrical oscillator," *IEEE Trans. Microw. Theory Techn.*, vol. 18, no. 5, pp. 967–9, May 1970.
[35] J. de Cos, A. Suárez, F. Ramírez, "Analysis of oscillation modes in free-running ring oscillators," *IEEE Trans. Microw. Theory Techn.*, vol. 60, no. 10, pp. 3137-3150, Oct., 2012.
[36] F. Ramirez, M. Ponton, S. Sancho and A. Suarez, "Stability Analysis of Oscillation Modes in Quadruple-Push and Rucker's Oscillators," *IEEE Trans. Microw. Theory Techn.*, vol. 56, no. 11, pp. 2648-2661, Nov. 2008.
[37] R. G. Freitag, "A unified analysis of MMIC power amplifier stability," *1992 IEEE MTT-S Int. Microw. Symp. (IMS)*, Alburquerque, USA, 1992, pp. 297-300.
[38] A. Suárez, E. Fernández, F. Ramírez, S. Sancho, "Stability and bifurcation analysis of self-oscillating quasi-periodic regimes," *IEEE Trans. Microw. Theory Techn.*, vol. 60, no. 3 , pp. 528-541,Mar. , 2012.
[39] A. Suárez and F. Ramírez, " Analysis of stabilization circuits for phase-noise reduction in microwave oscillators," *IEEE Trans. Microw. Theory Techn.*, vol. 53, pp. 2743-2751, Sept., 2005.
[40] M. Pontón, A. Suárez, "Wireless injection locking of oscillator circuits," *IEEE Trans. Microw. Theory Techn.*, vol. 64, no. 12, pp. 1-15, Dec., 2016.
[41] J. M. Paillot, J. C. Nallatamby, M. Hessane, R. Quéré, M. Prigent and J. Rousset, "A general program for steady state, stability, and FM noise analysis of microwave oscillators," *IEEE MTT Symposium*, 1990, pp. 1287–1290.
[42] V. Rizzoli, F. Mastri and D. Masotti, "General noise analysis of nonlinear microwave circuits by the piecewise harmonic balance technique," *IEEE Trans. Microw. Theory Techn.*, vol. 42, no. 5, pp. 807–819, May, 1994.

Silvia Hernández (S'17) was born in the Canary Islands, Spain. She received her M.S. degree in Telecommunication Engineering from the University of Las Palmas de Gran Canaria, Canary Islands, Spain, in 2015. The same year, she entered the Institute for the Technological Development and Innovation in Communications, University of Las Palmas de Gran Canaria, as a research assistant. In 2016, she joined the Communications Engineering Department, University of Cantabria, where she is currently working towards her Ph.D. degree.

Her research interests include stability, phase-noise analysis and the study of new methods for the analysis and design of nonlinear microwave circuits.

Almudena Suárez (M'96-SM'01-F'12) was born in Santander, Spain. She received the degree in electronic physics and the Ph.D. degree from the University of Cantabria, Santander, Spain, in 1987 and 1992, respectively, and the Ph.D. degree in electronics from the University of Limoges, France, in 1993. At present, she is a Full Professor at the University of Cantabria, and a member of its Communications Engineering Department. She has authored the book *Analysis and design of autonomous microwave circuits* for the publisher IEEE–Wiley and co–authored the book *Stability analysis of microwave circuits* for the publisher Artech–House. She belongs to the technical committees of the IEEE International Microwave Symposium and European Microwave Conference. She was an IEEE Distinguished Microwave Lecturer for the period 2006–2008. She is an associate editor of the IEEE Microwave Magazine. She is a member of the Board of Directors of EuMA and the Editor in Chief of International Journal of Microwave and Wireless Technologies from Cambridge University Press.